Common Mode Power Control of Three-Phase Inverter for Auxiliary Load without Access to Neutral Point

N.B. When citing this work, cite the original published paper.

(article starts on next page)

Common Mode Power Control of Three-Phase Inverter for Auxiliary Load without Access to Neutral Point

Junfei Tang, *Student Member*, *IEEE*, Daniel Pehrman, *Student Member*, *IEEE*,
Georgios Mademlis, *Student Member*, *IEEE*, and Yujing Liu, *Senior Member*, *IEEE*.

Abstract – **The purpose of this study is to investigate the potential of obtaining an auxiliary dc output from the common mode switching harmonics of a three-phase inverter without access to the neutral point of the ac load. To achieve this, the control of common mode switching harmonics with space vector modulation is proposed. With this control, common mode switching harmonics can be regulated independently from the differential mode power flow to the main three-phase load. To physically implement the common mode power flow, a harmonic extraction circuit is placed in parallel with the main three-phase load. The extraction circuit is formed by series-connected inductance and capacitance. Due to the LC series resonance and the mutual coupling of the inductance, only common mode switching harmonics can pass through the extraction circuit. The extracted harmonics are then rectified and delivered to the auxiliary dc output. The control and topology are verified in both simulations and experiments. In the end, it is shown in experiments that there is no significant difference of the inverter efficiency after the auxiliary dc load is connected. This method can be used for instance to drive an ac machine while charging a low voltage battery or powering a compressor simultaneously.**

Index Terms – **Power electronics, switching harmonics, common mode, zero-sequence.**

I. INTRODUCTION

Electromobility and renewable power generation have become popular due to increasing concerns regarding climate change [1]. In these applications, power electronic converters are widely used for transferring power between electrical machines, grid and batteries. It is common that an ac machine is driven while an auxiliary dc load needs to be powered simultaneously [2] [3] [4]. This auxiliary dc load can be a low voltage battery or a compressor for instance. Usually the main ac load and the auxiliary dc load are powered by separated converters, which complicates the system and increases the cost.

Therefore, it becomes valuable to investigate the potential of obtaining an auxiliary dc output in parallel with the ac output of the same inverter. This idea is theoretically possible. In the switching patterns of space vector modulation (SVM), there exist both differential mode (DM) and common mode (CM) voltage components. It is the line voltages, i.e. the DM components, that deliver power to the ac load, while the zero-sequence voltages, i.e. the CM components, are not contributing to ac power transfer. Thus, by extracting and rectifying the CM switching harmonics from the inverter ac output, it would become possible to obtain an auxiliary dc output from the same inverter. The reason to focus on the CM switching harmonics instead of the SVM third harmonic is that, during the acceleration and deceleration of a machine, the frequency of the third harmonic will vary, while the frequency of CM switching harmonics is fixed which is easier to extract.

Junfei Tang, Daniel Pehrman, Georgios Mademlis and Yujing Liu are with the Department of Electrical Engineering, Chalmers University of Technology, Gothenburg, Sweden (email: junfei.tang@chalmers.se; daniel.pehrman@chalmers.se; georgios.mademlis@chalmers.se; yujing.liu@chalmers.se).

Analysis on CM switching harmonics has been pursued in previous studies. In [5], a zero-vector redistribution technique is proposed to suppress zero-sequence current in open-winding permanent magnet synchronous motor. In [6] and [7], a hybrid SVM is developed to instantaneously eliminate zero-sequence voltages. The proposed method is used in dual-fed open-end winding PMSM for aircraft. In [8], an optimized zero-sequence voltage injection method is proposed to eliminate circulating current in parallel-connected three-level converters. In [9], the effects of carrier wave phase shifts on circulating current of parallel-connected inverters are studied. Among these studies, the focus is mainly on the elimination of CM power flow. In [10], a generic multilevel SVPWM technique is proposed to eliminate the CM voltages for multiphase drives. In the technique, only switching states that produce zero CMV are applied.

Furthermore, the idea of utilizing CM voltage components to obtain an auxiliary dc output is proposed in a few studies. In [11], the CM components are extracted by accessing the neutral point of a three-phase load. In [12], additional circuit branches are added to control the CM power flow. The schematic diagram of the circuit is shown in Fig. 1 (a). In [13], a neutral point power transfer topology for low voltage battery charging is proposed. The circuit diagram is shown in Fig. 1 (b). An additional asymmetric half bridge which acts as a bidirectional buck converter is connected to the neutral point of the three-phase winding. In [14], the feasibility to integrate the charging of 12 V battery to the 48 V drivetrain in electromobility is evaluated. The focus is on charging efficiency in regeneration, motoring and idle modes of the machine operation.
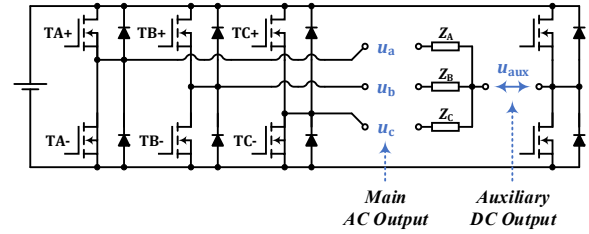
(a) Schematic diagram of the circuit proposed in [12]
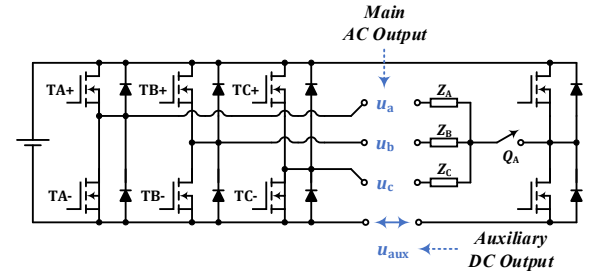
(b) Schematic diagram of the circuit proposed in [13] and evaluated in [14]

Fig. 1   Schematic diagrams of the circuits proposed in previous studies which utilize the neutral point of the three-phase load to extract common mode switching harmonics for auxiliary power output

However, there are drawbacks of these proposed topologies. Firstly, to extract the CM switching harmonics, the neutral point of the three-phase windings needs to be connected. However, the neutral point is not always accessible in the machines that are already in use, and to have the neutral point accessible in new machines would increase the cost. Secondly, before the harmonic currents reach the neutral point, they need to pass through the machine windings. This would introduce torque ripples and additional copper and iron-core losses to the machine. Consequently, the machine performance would deteriorate. Therefore, it is preferable to extract the CM switching harmonics and make use of them without accessing the neutral point.

The purpose of this study is to investigate the potential of obtaining an auxiliary dc output from the inverter switching harmonics without accessing the neutral point of the ac load. To realize this, three key challenges are to be confronted. Firstly, the CM switching harmonics need to be under independent control from the DM power flow to the ac load, so that the auxiliary dc output can be adjusted according to the demand and the original functionality of the inverter is not sacrificed. Secondly, a circuit topology needs to be designed so that CM harmonics can be extracted and delivered to the auxiliary dc output. Thirdly, the impact of the CM harmonic extraction on the inverter needs to be investigated.

To tackle these challenges, the control of CM switching harmonics with SVM is proposed. With this control, CM switching harmonics can be regulated independently from the DM power flow to the main ac load. To physically implement the CM power flow to the auxiliary dc load, a harmonic extraction circuit is designed and placed in parallel with the ac load as shown in Fig. 2. The circuit and control are verified in simulations and experiments. Finally, the impact on inverter efficiency is investigated.
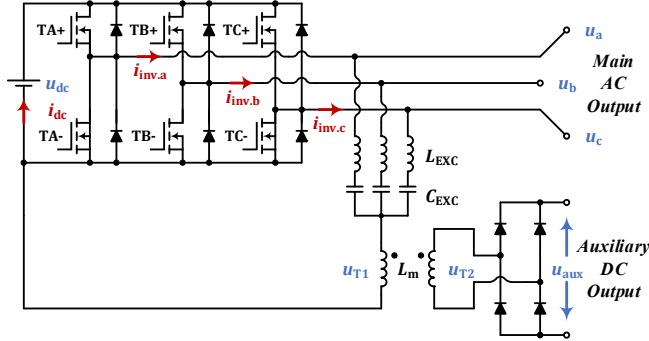

Fig. 2 Schematic diagram of the proposed circuit which utilizes common mode switching harmonics for auxiliary power output

The advantage of the proposed method is that, both a main AC load and an auxiliary DC load can be simultaneously powered from only one inverter, which simplifies the system and saves the cost. The novelty of this work is that the advantage can be achieved without access to the neutral point of the main AC load. Due to the page limit, the technical details regarding dynamic control, switching frequency optimization, and thermal modelling are not covered in the article.

II. CONTROL OF CM SVM SWITCHING HARMONICS

The switching harmonics in SVM patterns consist of both CM and DM components [15]. In this section, the SVM switching harmonics, especially the CM contents, are analyzed. As shown in Fig. 3 (a), a two-level three-phase inverter with u_{dc} as the dc-link voltage is considered in this study. However, the analysis can be extended to converters with multi-level and multi-phase. The SVM hexagon on αβ-plane is shown in Fig. 3 (b), where the entire hexagon is divided into six sectors [16].
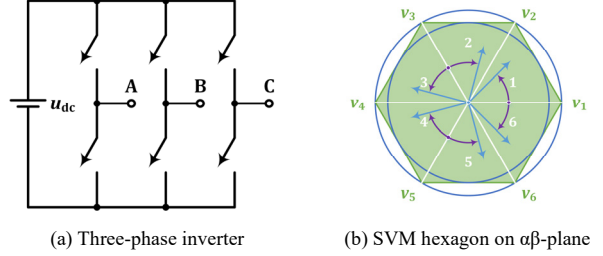

(a) Three-phase inverter   (b) SVM hexagon on αβ-plane

Fig. 3 Three-phase inverter with SVM

A. Common- and Differential mode Contents of SVM States

The vectors of SVM states can be defined as
$$\boldsymbol{V}_{SVM} = [v_0 \quad v_1 \quad v_2 \quad v_3 \quad v_4 \quad v_5 \quad v_6 \quad v_7]$$
$$= \begin{bmatrix} 0 & 1 & 1 & 0 & 0 & 0 & 1 & 1 \\ 0 & 0 & 1 & 1 & 1 & 0 & 0 & 1 \\ 0 & 0 & 0 & 0 & 1 & 1 & 1 & 1 \end{bmatrix}. \quad (1)$$
A duty cycle vector can be defined correspondingly
$$\boldsymbol{d}_{SVM} = [d_0 \quad d_1 \quad d_2 \quad d_3 \quad d_4 \quad d_5 \quad d_6 \quad d_7]^T. \quad (2)$$
Therefore, the duty cycle vector for the three phases are
$$\boldsymbol{d}_{abc} = [d_a \quad d_b \quad d_c]^T = \boldsymbol{V}_{SVM} \boldsymbol{d}_{SVM}. \quad (3)$$
Hence the three-phase output voltages can be described as
$$\boldsymbol{u}_{abc} = [u_a \quad u_b \quad u_c]^T = u_{dc} \boldsymbol{d}_{abc}. \quad (4)$$
With amplitude-invariant Clarke transform [17], the voltage vector can be transformed from abc-frame to αβγ-frame
$$\boldsymbol{u}_{\alpha\beta\gamma} = [u_\alpha \quad u_\beta \quad u_\gamma]^T = \boldsymbol{T}_{abc \to \alpha\beta\gamma} \boldsymbol{u}_{abc} \quad (5)$$
where $\boldsymbol{T}_{abc \to \alpha\beta\gamma}$ is the transform matrix. In αβγ-frame, the DM and CM components can be clearly identified. The DM components are described as u_α and u_β, whereas the CM component is described as u_γ.

If the mid-point of the inverter dc-link is regarded as the reference ground, then by using (5), the eight SVM state vectors in both abc- and αβγ-frame can be summarized as in TABLE I. The states are illustrated as green circles in 3D αβγ-frame in Fig. 4. As can be noticed, none of the states are located on the αβ-plane. The projection of the state vectors from the 3D space to the αβ-plane form a hexagon in green, which is actually the SVM hexagon in Fig. 3 (b). The state vectors in 3D space form a hexahedron. All six faces are rhombi. The upper three rhombi are shown in yellow in Fig. 4 (a) while the lower three are shown in blue in Fig. 4 (b). From the table and the figure, the following conclusions can be drawn: (1) for all the eight states, $u_\gamma \neq 0$ is valid. This means there is no state that gives purely DM components; (2) only for v_0 and v_7, $\|u_{\alpha\beta}\| = 0$ is valid, whereas for all the six other states, $\|u_{\alpha\beta}\| \neq 0$ is valid.

TABLE I   SVM switching states in abc and αβγ coordinates

State Vector			$\dfrac{u_a}{u_{dc}}$	$\dfrac{u_b}{u_{dc}}$	$\dfrac{u_c}{u_{dc}}$	$\dfrac{u_\alpha}{u_{dc}}$	$\dfrac{u_\beta}{u_{dc}}$	$\dfrac{u_\gamma}{u_{dc}}$
CM		v_0	$-1/2$	$-1/2$	$-1/2$	0	0	$-1/2$
DM	odd	v_1	$1/2$	$-1/2$	$-1/2$	$2/3$	0	$-1/6$
	even	v_2	$1/2$	$1/2$	$-1/2$	$1/3$	$1/\sqrt{3}$	$1/6$
	odd	v_3	$-1/2$	$1/2$	$-1/2$	$-1/3$	$1/\sqrt{3}$	$-1/6$
	even	v_4	$-1/2$	$1/2$	$1/2$	$2/3$	0	$1/6$
	odd	v_5	$-1/2$	$-1/2$	$1/2$	$-1/3$	$-1/\sqrt{3}$	$-1/6$
	even	v_6	$1/2$	$-1/2$	$1/2$	$1/3$	$-1/\sqrt{3}$	$1/6$
CM		v_7	$1/2$	$1/2$	$1/2$	0	0	$1/2$
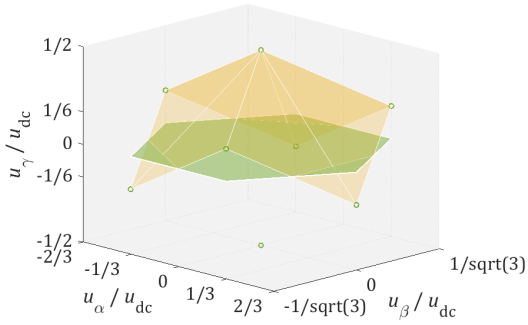
(a) Upper three rhombi & SVM hexagon
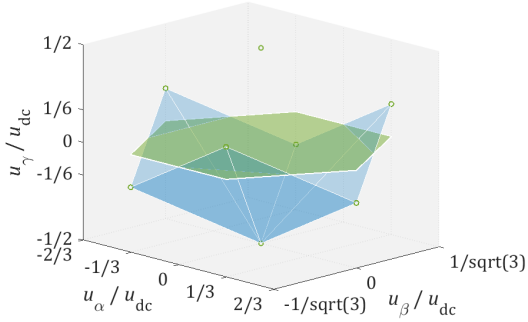
(b) Lower three rhombi & SVM hexagon

Fig. 4   SVM switching states in αβγ-frame

Usually, v_0 and v_7 are classified as zero states since they only give CM component, while the other six states are classified as active states since they give DM components. Furthermore, among all the active states, v_1, v_3, v_5 are with odd number of 1 and hence can be classified as odd states, while v_2, v_4, v_6 can be classified as even states. This categorization is proposed in [6] and it is used here for the convenience of analysis later.

B. Determination of Duty Cycles in SVM

The duty cycles of three phases, d_a, d_b and d_c, can be determined from the duty cycles of the switching states, d_0, d_1, d_2 until d_7, as summarized in TABLE II.

TABLE II   Duty cycles of three phases

Sector	d_a	d_b	d_c
1	$d_1 + d_2 + d_7$	$d_2 + d_7$	d_7
2	$d_2 + d_7$	$d_2 + d_3 + d_7$	d_7
3	d_7	$d_3 + d_4 + d_7$	$d_4 + d_7$
4	d_7	$d_4 + d_7$	$d_4 + d_5 + d_7$
5	$d_6 + d_7$	d_7	$d_5 + d_6 + d_7$
6	$d_6 + d_1 + d_7$	d_7	$d_6 + d_7$

To obtain d_0 until d_7, firstly the sector where the vector is located needs to be identified. Thereafter, an angle $\theta_{60°}$ can be defined to describe the location of the vector within each 60° hexagon sector. The calculation of $\theta_{60°}$ is illustrated in Fig. 3 (b). The voltage vectors in each sector are marked in blue while the corresponding $\theta_{60°}$ is marked in purple. The calculation of $\theta_{60°}$ can be formulated by using $\theta_{360°}$, which is the absolute angle in 2π, as

$$\theta_{60°} = \begin{cases} \theta_{360°} & sector\ 1 \\ 2\pi/3 - \theta_{360°} & sector\ 2 \\ \theta_{360°} - 2\pi/3 & sector\ 3 \\ 4\pi/3 - \theta_{360°} & sector\ 4 \\ \theta_{360°} - 4\pi/3 & sector\ 5 \\ 2\pi - \theta_{360°} & sector\ 6 \end{cases} \quad (6)$$

Then the duty cycles of odd and even states can be formulated

$$d_{odd} = m_a \cos(\theta_{60°} + \pi/6)\ , d_{even} = m_a \sin\theta_{60°}. \quad (7)$$

The sum of duty cycles of all active states can be defined as

$$d_{DM} = \sum_{i=1}^{6} d_i = d_{odd} + d_{even} = m_a \cos(\theta_{60°} - \pi/6) \quad (8)$$

while the remaining can be defined as d_{CM}

$$d_{CM} = 1 - d_{DM} = 1 - m_a \cos(\theta_{60°} - \pi/6) \quad (9)$$

which is shared between v_0 and v_7

$$d_{CM} = d_0 + d_7. \quad (10)$$

In default SVM scheme, d_{CM} is evenly shared between v_0 and v_7. However, there are other possibilities, which will be described in the next section.

C. Parameters to Determine SVM Switching Patterns

In this study, two disciplines are respected to determine the SVM switching pattern: (1) the line voltages implemented by the SVM pattern in average of a switching cycle should follow the request, and (2) maximally one turn-on switching action and one turn-off switching action of each half-bridge branch are allowed within each switching cycle. The first discipline is the basic requirement for the inverter to drive the three-phase load, whereas the second is to avoid unnecessary switching losses.

When both disciplines are fulfilled, a specific SVM switching pattern can be determined by three parameters: amplitude modulation index m_a, distribution of CM state vector k_7 and interleave shift α.

1) Amplitude Modulation Index m_a

To form a continuous rotation of the projected voltage vector on αβ-plane $u_{\alpha\beta}$, the maximum possible length of the vector is

the radius of the inscribed circle of the SVM hexagon

$$u_{\max} = \max\{\|u_{\alpha\beta}\|\} = u_{dc} / \sqrt{3}. \qquad (11)$$

The amplitude modulation index is used to describe the length of the voltage vector, and it can be defined as the radius in per unit by taking $u_{\max}$ as the reference base

$$m_a = \|u_{\alpha\beta}\| / u_{\max} = \sqrt{3} \cdot \|u_{\alpha\beta}\| / u_{dc}. \qquad (12)$$

A certain value of m_a indicates a certain level of line voltages. The line voltage rms can be determined as

$$U_{line.rms} = m_a \cdot u_{dc} / \sqrt{2}. \qquad (13)$$

In this study, linear modulation range, m_a between 0 and 1, is considered. In case of overmodulation, (7) becomes not valid anymore. However, the common mode harmonics are decided in the same way from the duty cycles of the switching states. Thus, the conclusions thereafter are still valid.

2) Distribution of CM State Vector k_7

Assuming all phases share the same triangular carrier wave, based on the algorithm introduced in Section II.B, d_1, d_2, d_3 until d_6 are decided by m_a. Hence if m_a is decided, according to (8) and (9), d_{DM} and d_{CM} are decided consequently. However, as for how d_{CM} is shared between v_0 and v_7, there are many possibilities. This is described by a distribution factor k_7 in this study

$$k_7 = d_7/d_{CM} \in [\, 0\, ,1\,] \qquad (14)$$

which means the share of d_7 over d_{CM}. A higher k_7 means to shift all phase voltage references up by the same amount while the line voltage references are kept constant. In traditional SVM, d_0 and d_7 share d_{CM} equally, which means $k_7 = 0.5$. In this study, k_7 is allowed to vary between 0 and 1.

3) Interleave Shift α

The interleave shift in this study means to introduce phase difference between triangular carrier waves in SVM. An interleave shift will not change the average voltage in each phase but will change the time instant when the switching actions occur. Thus, the line voltages will be the same and this will not violate the SVM disciplines.

D. Control of Switching Harmonic Contents

Fourier analysis can be performed to quantify the harmonic contents for each switching cycle. For one single phase leg, considering a waveform centered at zero time instant, then the amplitude of the cosine component at harmonic order h is

$$a_h = \frac{2 \cdot \sin(h\pi d) - \sin(h\pi)}{\pi \cdot h} \qquad (15)$$

while the amplitude of the sine component b_h is zero due to half-wave symmetry. The complex form is therefore

$$c_h = a_h + jb_h = \frac{2 \cdot \sin(h\pi d) - \sin(h\pi)}{\pi \cdot h}. \qquad (16)$$

When an interleave shift α is introduced, the complex Fourier component of this phase becomes

$$c_h = \frac{2}{\pi} \frac{\sin(h\pi d) - \sin(h\pi)}{h} e^{j\alpha}. \qquad (17)$$
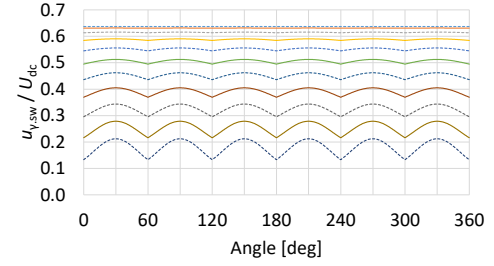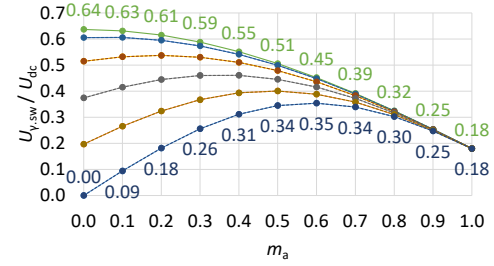
Considering the waveform of Phase B as centered at zero and
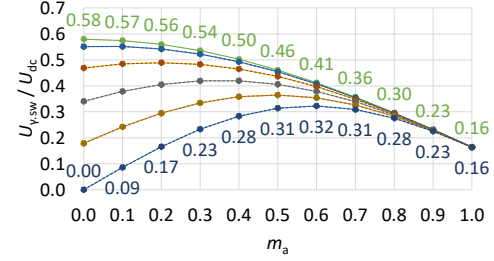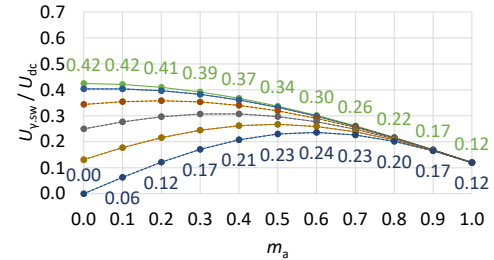
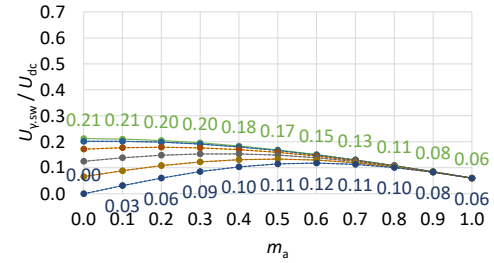Fig. 5 Switching harmonics in each switching cycle ($k_7 = 0$, $\alpha = 0°$)

(a) $\alpha = 0°$

(b) $\alpha = 30°$

(c) $\alpha = 60°$

(d) $\alpha = 90°$

Fig. 6 Switching harmonics in average ($m_a = 0.0$ - 1.0, $k_7 = 0.0$ - 1.0)

Phase A leading B by α while Phase C lagging B by α, then the CM content can be formulated as

$$\frac{u_{\gamma.\text{sw}}}{u_{\text{dc}}} = \frac{2}{\pi} \frac{\sin(\pi d_a)\cos\alpha + \sin(\pi d_b) + \sin(\pi d_c)\cos\alpha}{3}. \quad (18)$$

The time-domain waveforms of the switching frequency component with $k_7 = 0$ and $\alpha = 0°$ are shown in Fig. 5. 360 points are calculated in each fundamental cycle, i.e. 1 point per degree. As can be noticed, with a lower value of m_a, the average over one fundamental cycle is higher and the ripple is lower.

The average values of the switching frequency component over one fundamental cycle with $\alpha = 0°$, 30°, 60° and 90° are shown in Fig. 6. The average value of the component is not linear with respect to m_a. An increasing α leads to a decreasing average value. At $\alpha = 30°$, 60°, 90° and 120°, all the average values in the map decrease to 91.1%, 73.2%, 33.3% and 0% of that at $\alpha = 0°$. This can be explained analytically. The average value of the switching harmonic content over one fundamental cycle can be calculated as

$$\frac{U_{\gamma.\text{sw}}}{U_{\text{dc}}} = \frac{1}{2\pi} \int_0^{2\pi} \frac{u_{\gamma.\text{sw}}}{u_{\text{dc}}} d\theta. \quad (19)$$

Due to three-phase symmetry,

$$\int_0^{2\pi} \sin(\pi d_a)\, d\theta = \int_0^{2\pi} \sin(\pi d_b)\, d\theta = \int_0^{2\pi} \sin(\pi d_c)\, d\theta. \quad (20)$$

Hence the average can be calculated by considering only one phase and using a scaling factor $\frac{1+2\cdot\cos\alpha}{3}$

$$\int_0^{2\pi} \frac{u_{\gamma.\text{sw}}}{u_{\text{dc}}} d\theta = \frac{1 + 2\cdot\cos\alpha}{3} \frac{2}{\pi} \int_0^{2\pi} \sin(\pi d_a)\, d\theta. \quad (21)$$

With $\alpha = 30°$, 60°, 90° and 120°, the scaling factor $\frac{1+2\cdot\cos\alpha}{3}$ gives 0.911, 0.732, 0.333 and 0 which are consistent with Fig. 6. In addition, the integrations of $\sin(\pi d_a)$ in sectors 1, 2 and 3 are equal to those in sector 6, 5 and 4 respectively due to symmetry. Therefore, (21) can be simplified as

$$\int_0^{2\pi} \sin(\pi d_a)\, d\theta = 2 \int_0^{\pi/3} \left\{ \begin{array}{c} \sin(\pi d_0) + \sin(\pi d_7) \\ + \sin[\pi(d_2 + d_7)] \end{array} \right\} d\theta. \quad (22)$$

It should be pointed out that, the derivations in (20) (21) (22) are based on the assumption that the three-phase voltages are balanced. In case of an unbalance condition in grid applications, the results presented in Fig. 5 and Fig. 6 need to be analyzed separately. However, if the three-phase voltages are balanced while the currents are not, then the SVM switching pattern is not affected. In this case, the derivations in (20) (21) (22) and the results presented in Fig. 5 and Fig. 6 are still valid.

III. EXTRACTION OF CM SVM SWITCHING HARMONICS

In this section, the principle of harmonic extraction is explained and then a model of the circuit is established. The validation of the circuit is presented in the next section.

A. Topology

The schematic diagram of the entire circuit is shown in Fig. 2. The output of the inverter is split into two branches. One branch goes to the main ac load, which can be an electrical machine or a grid for example. The other branch goes to a harmonic extraction circuit which blocks DM harmonics while lets CM harmonics pass. After the extraction circuit is a transformer. The transformer is used for galvanic isolation and is not necessary for the functionality of the extraction circuit. The secondary side of the transformer is connected to a full-bridge rectifier, and then to the auxiliary dc load. The auxiliary dc load can be a battery or compressor for example. The harmonic extraction circuit and the transformer form a resonance circuit. The resonance frequency is tuned to the switching frequency. Hence the CM switching harmonics are extracted and delivered to the auxiliary dc load.

B. Harmonic Extraction Circuit

The extraction circuit is built to only let the CM switching harmonics pass through. To realize this, the circuit consists of a CM-passing coil which only lets CM components pass through, and capacitors connected in series which resonate with the coil. The resonance is tuned at the switching frequency, so that only the CM switching harmonics are able to pass through.

1) CM-Passing Coil

With the positive direction of coil currents defined in Fig. 7 (a), three-phase currents can be decomposed into CM and DM components. The CM part is the average of the three currents

$$i_{\text{CM}} = (i_a + i_b + i_c)/3 \quad (23)$$

where i_a, i_b, i_c are the three-phase currents in the extraction circuit and i_{CM} is the CM component of them. The remaining part is the DM components

$$\boldsymbol{i}_{\text{DM}} = \boldsymbol{i}_{\text{abc}} - \boldsymbol{i}_{\text{CM}} \quad (24)$$

where

$$\boldsymbol{i}_{\text{DM}} = \begin{bmatrix} i_{\text{DM.a}} \\ i_{\text{DM.b}} \\ i_{\text{DM.c}} \end{bmatrix}, \boldsymbol{i}_{\text{abc}} = \begin{bmatrix} i_a \\ i_b \\ i_c \end{bmatrix}, \boldsymbol{i}_{\text{CM}} = \begin{bmatrix} i_{\text{CM}} \\ i_{\text{CM}} \\ i_{\text{CM}} \end{bmatrix} \quad (25)$$

$i_{\text{DM.a}}$, $i_{\text{DM.b}}$, $i_{\text{DM.c}}$ are the three-phase DM component currents in the extraction circuit. Hence from (23) and (24), the sum of DM currents is zero

$$i_{\text{DM.a}} + i_{\text{DM.b}} + i_{\text{DM.c}} = 0. \quad (26)$$

There are two ways to wind three-phase coils symmetrically as shown in Fig. 7 (b) and (c). The flux linkages generated by the three-phase coils can be formulated as

$$\boldsymbol{\psi}_{\text{abc}} = \boldsymbol{L}_{\text{abc}}\, \boldsymbol{i}_{\text{abc}} \quad (27)$$

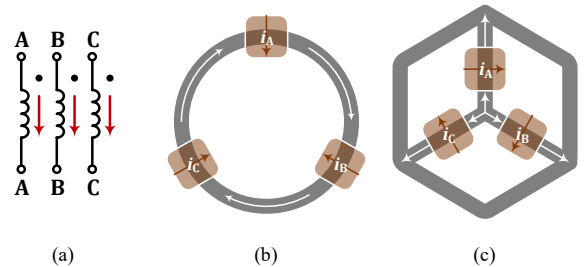where $\boldsymbol{\psi}_{\text{abc}}$ is the flux linkage vector and $\boldsymbol{L}_{\text{abc}}$ is the

Fig. 7   DM- and CM-passing coils
(a) Reference direction of currents (b) DM-Passing coil (c) CM-Passing coil

inductance matrix

$$\boldsymbol{\psi}_{abc} = \begin{bmatrix} \psi_a \\ \psi_b \\ \psi_c \end{bmatrix}, \boldsymbol{L}_{abc} = \begin{bmatrix} L_s & L_m & L_m \\ L_m & L_s & L_m \\ L_m & L_m & L_s \end{bmatrix}. \quad (28)$$

TABLE III   DM- and CM-passing coils

	DM-Passing Coil	CM-Passing Coil
L_m	L_M	$-L_M/2$
L_s	$L_M + L_\sigma$	$L_M + L_\sigma$
$\boldsymbol{L}_{abc}$	$\begin{bmatrix} L_M + L_\sigma & L_M & L_M \\ L_M & L_M + L_\sigma & L_M \\ L_M & L_M & L_M + L_\sigma \end{bmatrix}$	$\begin{bmatrix} L_M + L_\sigma & -L_M/2 & -L_M/2 \\ -L_M/2 & L_M + L_\sigma & -L_M/2 \\ -L_M/2 & -L_M/2 & L_M + L_\sigma \end{bmatrix}$
L_{CM}	$L_\sigma + 3L_M$	L_σ
L_{DM}	L_σ	$L_\sigma + 3L_M/2$

Due to symmetry, all the self-inductances L_s are equal, so are the mutual inductances L_m. The self-inductances are the sum of the magnetizing inductance L_M and the leakage inductance L_σ

$$L_s = L_M + L_\sigma. \quad (29)$$

The magnetizing inductances L_M indicate the ability of a coil for generating flux that links all other coils. The generated flux can be shared by other coils in series, as shown in Fig. 7 (b), or in parallel, as shown in Fig. 7 (c). The link between different coils is indicated by mutual inductances L_m.

In the case of CM current component,

$$\boldsymbol{\psi}_{CM} = \boldsymbol{L}_{abc}\,\boldsymbol{i}_{CM} = (L_s + 2L_m)\,\boldsymbol{i}_{CM}. \quad (30)$$

Thus the CM inductance is

$$L_{CM} = L_s + 2L_m. \quad (31)$$

In case of DM current component,

$$\boldsymbol{\psi}_{DM} = \boldsymbol{L}_{abc}\,\boldsymbol{i}_{DM} = (L_s - L_m)\,\boldsymbol{i}_{DM}. \quad (32)$$

Thus the DM inductance is

$$L_{DM} = L_s - L_m. \quad (33)$$

As for the arrangement in Fig. 7 (b), the main flux from one coil is shared by the other two in series. Thus, the mutual inductance equals magnetizing inductance

$$L_m = L_M. \quad (34)$$

As for the arrangement in Fig. 7 (c), the main flux is shared by the other two in parallel. Besides, the flux generated by each coil counteracts each other. Thus, the mutual inductance should be half of the magnetizing inductance with a minus sign

$$L_m = -L_M/2. \quad (35)$$

A Summary of these two winding arrangements is concluded in TABLE III. As can be noticed, by increasing L_M while minimizing L_σ, in case of Fig. 7 (b), CM components are blocked while DM components can pass. Hence it is a DM-passing coil. In case of Fig. 7 (c), the situation is the opposite, which means it is a CM-passing coil. In this study, the focus is to make use of the CM switching component. Thus, only a CM-passing coil is applied in this study.

2)   Resonance Circuit

A resonance can be formed by the CM-passing coil and the capacitance in series. The series-resonance is designed to extract the component at the switching frequency. The equivalence of the circuit from three-phase to single-phase in terms of the CM switching harmonic is illustrated in Fig. 8. The resistance in

three-phase can be regarded as being placed in parallel and becomes 1/3 in single-phase. The same applies for capacitance and inductance. The equivalent inductance in the CM circuit is the leakage inductance of the CM passing coil according to (29).
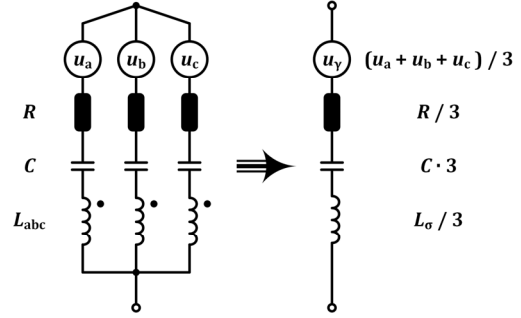

Fig. 8   Resonance circuit formed by the extraction circuit

C.   Rectifier and DC Load

The output of the transformer is connected to a rectifier. At the output of the rectifier is a dc load. The dc load can be capacitive or inductive as shown in Fig. 9. Due to the resonance formed by the CM-passing coil and the capacitors as shown in Fig. 8, the extraction circuit behaves as a band pass filter. Hence only the harmonic content at the switching frequency can pass through the extraction circuit and reach the input of the rectifier. In this case, the rectifier load can be represented as an equivalent

(a) Rectifier and capacitive load

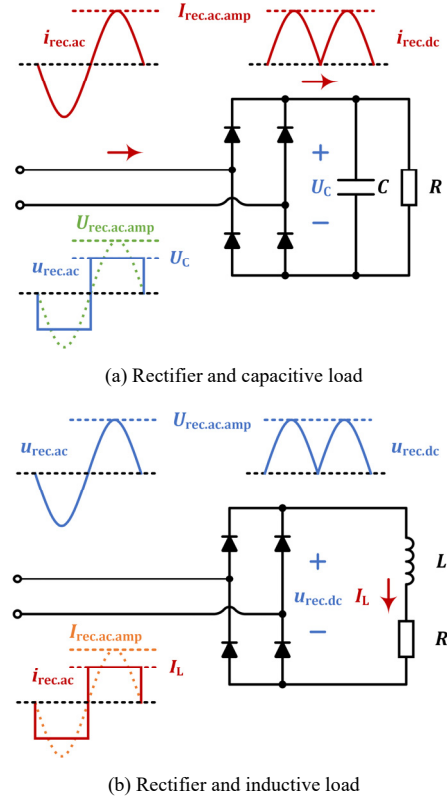
(b) Rectifier and inductive load

Fig. 9   Rectifier connected with capacitive or inductive load

resistance at the sinusoidal frequency [18].

In case of a capacitive dc load, the voltage U_C is kept constant in steady state as shown in Fig. 9 (a). The equivalent resistance can be calculated as

$$R_{\text{eq.C}} = \frac{U_{\text{rec.ac.amp}}}{I_{\text{rec.ac.amp}}} = \frac{4/\pi \cdot U_C}{\pi/2 \cdot I_R} = \frac{8}{\pi^2} \cdot \frac{U_C}{I_R} = \frac{8}{\pi^2} \cdot R. \quad (36)$$

In case of an inductive dc load, the current I_L is kept constant in steady state as shown in Fig. 9 (b). The equivalent resistance can be calculated as

$$R_{\text{eq.L}} = \frac{U_{\text{rec.ac.amp}}}{I_{\text{rec.ac.amp}}} = \frac{\pi/2 \cdot U_R}{4/\pi \cdot I_L} = \frac{\pi^2}{8} \cdot \frac{U_R}{I_L} = \frac{\pi^2}{8} \cdot R. \quad (37)$$

In the validation part, a capacitor is placed at the output of the rectifier. Therefore, it is considered as the capacitive case shown in Fig. 9 (a).

IV. Experimental Verification

An experimental setup is constructed to verify the control and circuit. Analytical results are calculated based on the modeling in Section III and compared with the experimental results. In the end, the impact on the inverter efficiency is investigated.

A. System Setup

The experimental setup is shown in Fig. 10. Code Composer Studio is used to program TMS320F28379 for controlling the three-phase inverter. The three-phase outputs of the inverter are split into two branches. One branch goes to the three-phase RL load whereas the other goes to the extraction circuit. Toroidal cores and litz wires are used to make the CM-passing coil. The toroidal cores are made of 3C90 ferrite which is cost-effective and suitable for frequencies up to 200 kHz [19]. The cross-section area of each core is 172 mm2. Three layers of cores are stacked on top of each other to avoid saturation. The capacitors used here are from the C-CAP series in CELEM with coaxial technology. The three capacitors are placed in one row and clamped between a copper plate on top and an aluminum plate on bottom. The currents passing through the three capacitors join at the copper plate, and the joint current goes to the transformer.

1) Three-Phase Inverter

The inverter is constructed by three silicon carbide power modules CAB450M12XM3. The parameters and operating condition of the inverter are shown in TABLE IV.

TABLE IV   Power Electronic Inverter Parameters

Parameter	Symbol	Value	Unit
DC-Link Voltage	U_{dc}	200	V
Sine Fundamental Frequency	f_{sin}	100	Hz
Switching Frequency	f_{sw}	30	kHz
Drain-Source Resistance	$R_{\text{ds.on}}$	2.6	mΩ
Anti-Parallel Diode Voltage Drop	V_F	4.7	V

2) Harmonic Extraction Circuit & Transformer

The parameters of the extraction circuit are shown in TABLE
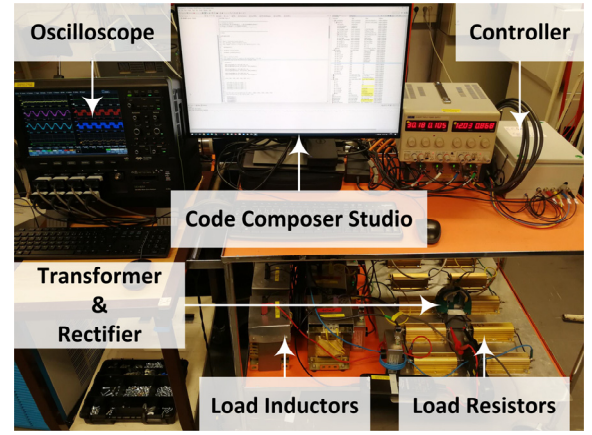
(a) Control panel, transformer, resistors and inductors
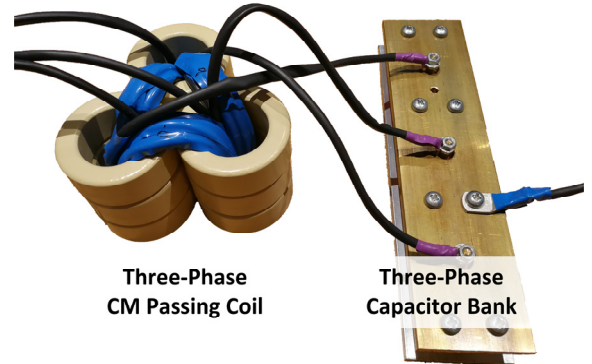
(b) Extraction circuit

Fig. 10   Experimental setup

V. The transformer used in this study is the one designed for brushless excitation in [20]. Litz wires with a strand diameter of 0.1 mm are used to form the windings on both sides. Pot cores with an airgap in between form the main flux path.

TABLE V   Electrical Parameters of Harmonic Extraction Circuit

Parameter	Symbol	Value	Unit
Resistance	R_{EXT}	47.73	mΩ
Self-Inductance	L_{EXT}	963.02	µH
Mutual-Inductance	M_{EXT}	959.19	µH
Capacitance	C_{EXT}	85	nF

TABLE VI   Electrical Parameters of Transformer

| Parameter	Symbol	Value	Unit
Primary Side Resistance	$R_{\text{T.1}}$	138	mΩ
Secondary Side Resistance	$R_{\text{T.2}}$	33.05	mΩ
Primary Side Self-Inductance	$L_{\text{T.1}}$	107.57	µH
Secondary Side Self-Inductance	$L_{\text{T.2}}$	16.66	µH
Mutual-Inductance	$L_{\text{T.m}}$	35.57	µH

3) Three-Phase RL Load & DC Load

The parameters of the three-phase RL load and DC load are listed in TABLE VII. The values are measured by powering the load from the inverter and applying FFT to the voltages and currents.

TABLE VII   Parameters of Three-Phase Load, Rectifier and DC Load

Parameter	Symbol	Value	Unit
AC Load Phase Resistance	R_{RL}	22.45	Ω
AC Load Phase Inductance	L_{RL}	32.38	mH
Diode Forward Voltage Drop	V_F	0.84	V
Auxiliary DC Load Capacitance	C_f	40	μF
Auxiliary DC Load Resistance	R_f	10.8	Ω
Auxiliary DC Load Inductance	L_f	83.05	mH

4) Resonance Profile

The diagram of resonance circuit is shown in Fig. 11 (a). The extraction circuit and the transformer primary side form the resonance circuit in no-load condition. In load condition, the transformer secondary side and the equivalent resistance of the rectifier with the dc load are in parallel with the transformer magnetizing inductance. The circuit parameters are referred to the primary side of the transformer. The total admittance is firstly calculated based on the circuit parameters, and then measured with an RLC meter. The results are shown in Fig. 11 (b). The vertical axis shows the admittances in logarithm. The resonance points are indicated in tabs, and the resonance frequencies are around 30 kHz. If a different switching frequency is selected, then the resonance circuit should be
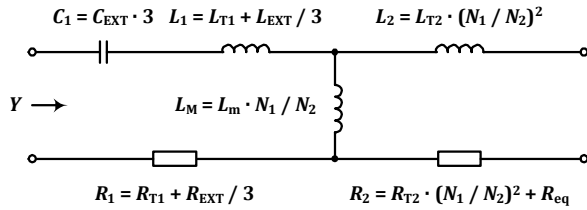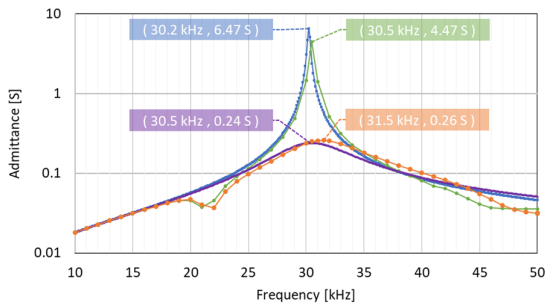
adjusted accordingly so that the resonance frequency equals the switching frequency. In load condition, the admittance curves become damped due to the load resistance. In this study, the switching frequency is fixed. If the switching frequency is variable in some applications, then the resonance profile should be designed in such a way that the amplification is relatively flat within the range of frequency variation.

B. Analytical Results

Assuming that (1) the inverter and rectifier are lossless, and (2) purely the CM harmonic at switching frequency passes the extraction circuit, then the auxiliary dc output voltage can be calculated using the profile in Fig. 6. Based on the circuit shown in Fig. 11 (a), the overall admittance of the CM branch at 30 kHz is 0.1975 S, including the CM extraction circuit, the transformer and the equivalent resistance of the dc load. 21% of the CM branch current goes to the dc-load whereas the remaining goes to the magnetizing branch of the transformer. From there, the auxiliary dc output voltage is calculated, and the profile is shown in Fig. 12. The maximum is reached in case of $k_7 = 0.5$ and $\alpha = 0°$. The shape of the profile changes when k_7 varies. The curves are symmetric with respect to $k_7 = 0.5$, e.g. the $k_7 = 0.4$ curve is the same as the $k_7 = 0.6$ curve. Adding shift α scales down the curves evenly which is consistent to (24).
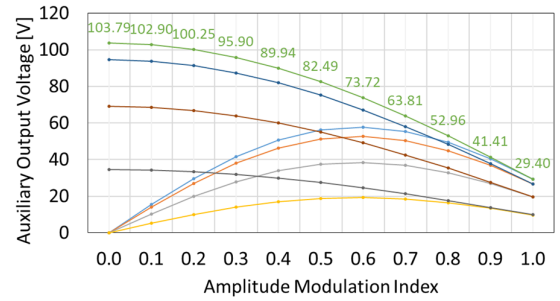

Fig. 12   Auxiliary voltage output in from theoretical calculations

C. Simulation Results

To verify the analytical results, the SVM algorithm is programmed in Simulink while the circuit topology is built by PLECS blocks. The simulation results are presented in Fig. 13. The shape of the profiles here closely follows the analytical curves shown in Fig. 12. In analytical calculations, the side-band CM harmonics are neglected, while in simulations, the side-band CM harmonics contribute to the auxiliary output. Hence, the curves in simulation results are slightly higher than those in analytical results.

$$C_1 = C_{EXT} \cdot 3 \quad L_1 = L_{T1} + L_{EXT} / 3 \quad L_2 = L_{T2} \cdot (N_1 / N_2)^2$$

$$L_M = L_m \cdot N_1 / N_2$$

$$R_1 = R_{T1} + R_{EXT} / 3 \qquad R_2 = R_{T2} \cdot (N_1 / N_2)^2 + R_{eq}$$

(a) Diagram of resonance circuit

Analytical: No Load   *Measurement: No Load*
Analytical: Load   *Measurement: Load*

(b) Admittance of the resonance circuit
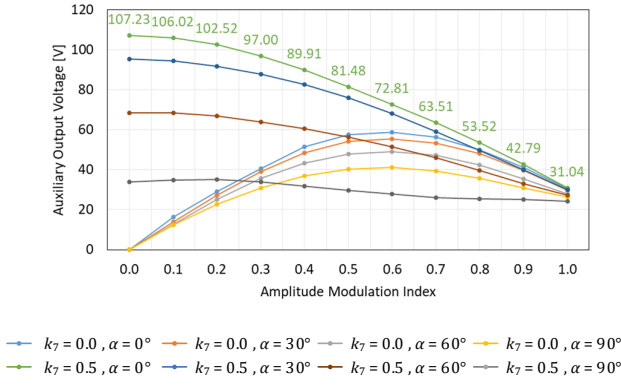
Fig. 11   Resonance analysis

Fig. 13 Auxiliary voltage output in circuit simulations

D. Experimental Results

Experimental results are shown in Fig. 14. The curves here closely follow the analytical results shown in Fig. 12. In analytical calculations, converter losses are neglected. Due to this, the auxiliary dc output voltage is overestimated. However, at the same time, the side-band CM harmonics contribute to the auxiliary output in experiments but not in analytical calculations. In the end, the discrepancies due to these two factors are more or less canceled. Hence the overall results in Fig. 14 closely follow the profiles in Fig. 12. As can be noticed, the auxiliary voltage output varies with all three parameters, m_a, k_7 and α. This further indicates the possibility to independently control the auxiliary voltage output utilizing CM switching harmonics by tuning k_7 and α without violating the control of three-phase power. In the plots of auxiliary dc output, the curves cover a wide voltage range at low levels of m_a. However, as m_a increases, all curves start to converge. At $m_a = 1.0$, there are minor differences between different curves. Besides, at this point, the voltage across the auxiliary dc load becomes very limited despite of whichever k_7 and α is chosen.
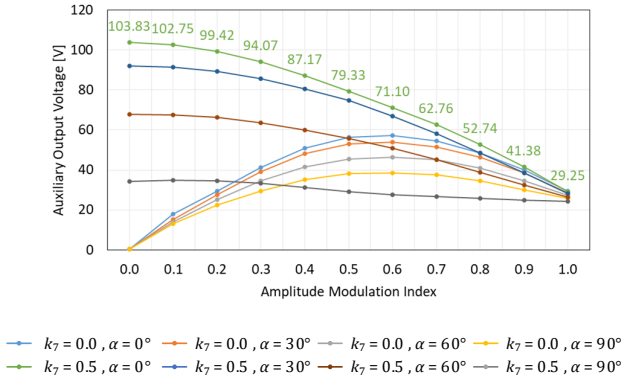

Fig. 14 Auxiliary voltage output in experiments

1) Original Case: $m_a = 0.5$ & $k_7 = 0.5$ & $\alpha = 0°$

With $k_7 = 0.5$ and $\alpha = 0°$, the inverter is operating with conventional SVM technique which gives the maximum amount of CM switching harmonics. The time domain waveforms in this case are measured. Waveforms in one electrical fundamental cycle are presented in Fig. 15. The inverter output currents $i_{INV.abc}$ shown in Fig. 15 (a) are split into the three-phase load currents $i_{RL.abc}$ and the harmonic extraction currents $i_{EXT.abc}$, as shown in Fig. 15 (b). $i_{RL.abc}$ are sinusoidal at 100 Hz while $i_{EXT.abc}$ contain switching harmonics. The harmonic currents going through the harmonic extraction circuit are all in phase. This indicates that the CM passing coil successfully blocks the DM components. The currents from three-phase harmonic extraction circuit join together and the sum goes to the transformer as shown in Fig. 15 (c). After the rectifier, the current becomes a dc quantity and goes to the dc load. The dc load current is 7.40 A.

(a) Inverter currents

(b) Three-phase load currents & extraction circuit currents
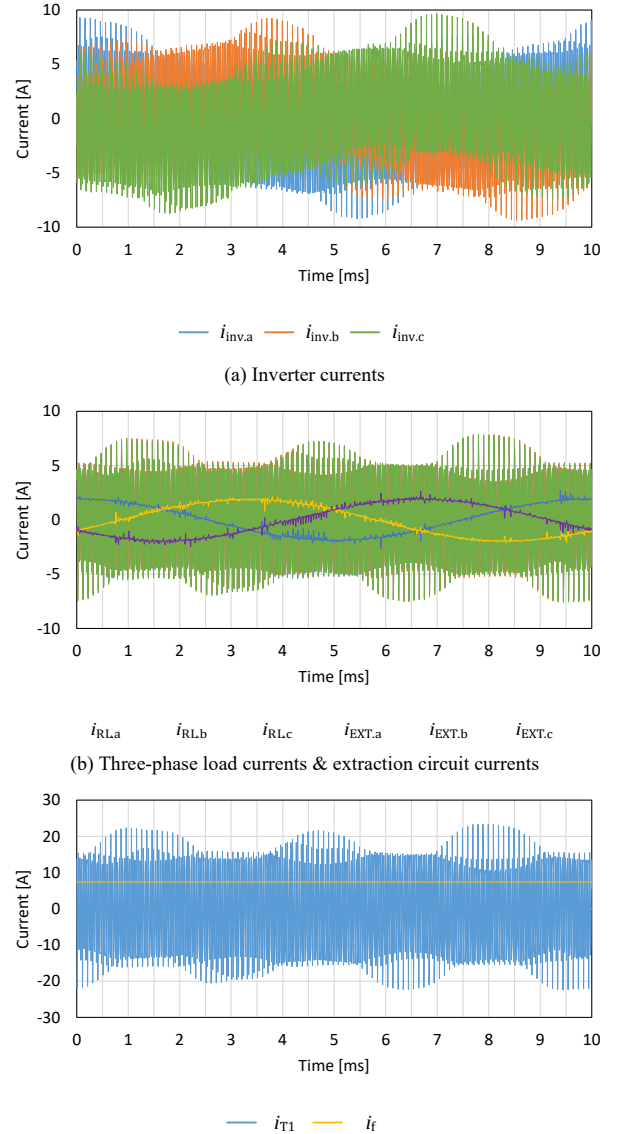
(c) Transformer primary side current & auxiliary load current

Fig. 15 Time-domain waveforms $m_a = 0.5$, $k_7 = 0.5$, $\alpha = 0°$

2)   Variation of k_7: $m_a = 0.5$ & $k_7 = 0.0$ & $\alpha = 0°$

With $k_7 = 0.0$ and $\alpha = 0°$, the CM switching harmonics are reduced by placing 100% inactive duty cycle to state vector v_7. The waveforms are shown in Fig. 16. As can be noticed, the three-phase RL currents in Fig. 16 (b) are the same as those in Fig. 15 (b). This indicates that the adjustment of CM switching contents does not affect the power going to the three-phase load at fundamental frequency. At the same time, the harmonic contents going through the extraction circuit reduce. This leads to cleaner waveforms of inverter output currents and lower amplitude of transformer current. Consequently, the current that reaches the dc load reduces. The dc load current is 5.26 A.
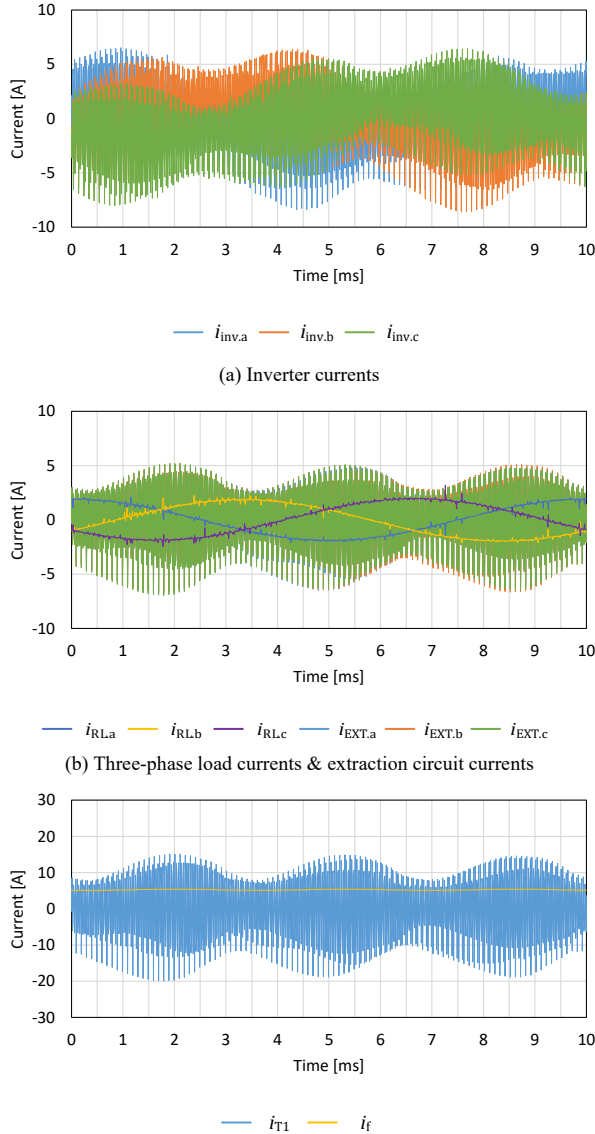
3)   Variation of α: $m_a = 0.5$ & $k_7 = 0.5$ & $\alpha = 90°$

With $k_7 = 0.5$ and $\alpha = 90°$, the CM switching harmonics are reduced by introducing interleave phase shift of carrier waves. The waveforms are shown in Fig. 17. The three-phase currents going to the RL load in this case are not affected either. Comparing with the case of $k_7 = 0.0$ and $\alpha = 0°$, the harmonic currents are reduced more significantly. Consequently, the current that reaches the dc load reduces to 2.75 A, 37% of the case with maximum CM switching harmonics. From analytical analysis, the CM harmonic at the switching frequency in this case are 33% of the maximum. These two percentage values are similar, which means the variation of power transfer can be roughly calculated by comparing CM switching harmonic contents.

(a) Inverter currents

(b) Three-phase load currents & extraction circuit currents

(c) Transformer primary side current & auxiliary load current

Fig. 16   Time-domain waveforms $m_a = 0.5$, $k_7 = 0.0$, $\alpha = 0°$

(a) Inverter currents

(b) Three-phase load currents & extraction circuit currents

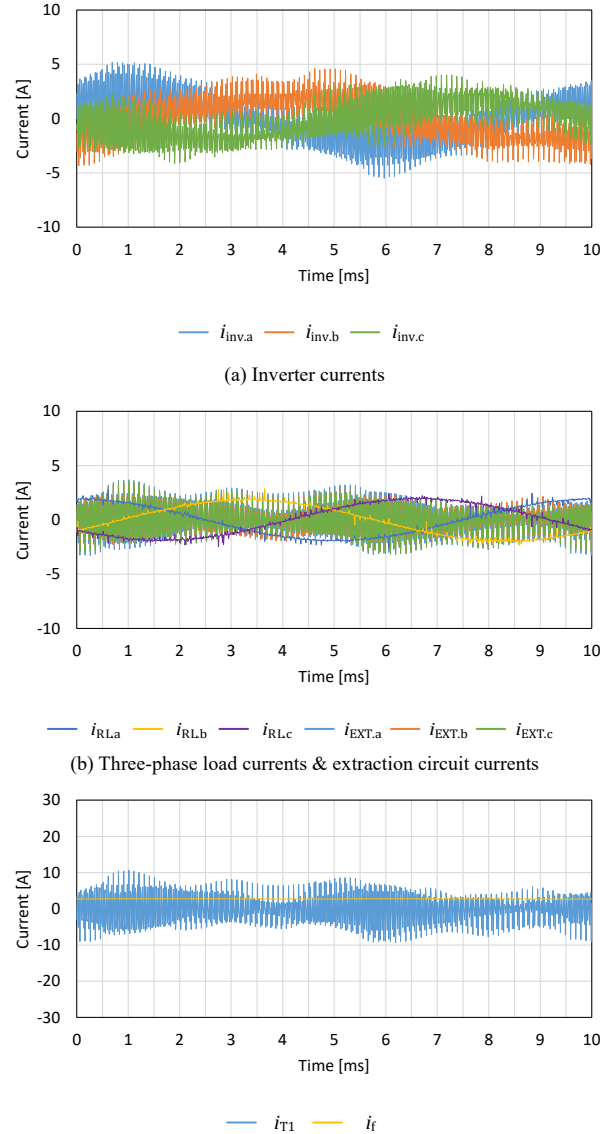(c) Transformer primary side current & auxiliary load current

Fig. 17   Time-domain waveforms $m_a = 0.5$, $k_7 = 0.5$, $\alpha = 90°$

4) Summary

The experimental results of the three presented cases are summarized in TABLE VIII. As can be noticed, the efficiency of the CM power flow branch, including extraction circuit, transformer and diode rectifier, reaches 93.18% in the traditional SVM case. However, when k_7 and α are regulated to decrease the CM power flow, the efficiency of the CM power flow branch decreases. This is due to two reasons. One reason is that, the diode rectifier becomes less efficient when the power flow decreases since the voltage drop across the diode PN junction is almost constant. The other reason is that, as the CM power flow decreases, the DM switching harmonics increase. The DM flux is then built in the CM-passing coil and this is why the DM power flow is prevented from passing the branch. However, at the same time, the DM flux also causes iron-core losses, and therefore the efficiency of the CM branch decreases.

TABLE VIII   Summary of Experimental Results of Three Typical Cases

Case					
	m_a		0.5	0.5	0.5
	k_7		0.5	0.0	0.5
	α		0º	0º	90º
DC-Link	AVG Voltage	[V]	201.13	201.08	201.12
	AVG Current	[A]	3.99	2.39	1.27
	Active Power	[W]	802.19	479.97	256.24
Main AC Load	RMS Voltage	[V]	64.91	64.84	89.06
	RMS Current	[A]	1.35	1.35	1.35
	Active Power	[W]	124.31	123.69	124.87
Auxiliary DC Load	AVG Voltage	[V]	79.33	56.32	29.23
	AVG Current	[A]	7.40	5.26	2.75
	Active Power	[W]	587.38	296.24	80.40
Inverter Efficiency		[%]	94.08	94.41	86.09
CM Branch Efficiency (including extraction circuit, transformer and diode rectifier)		[%]	93.18	89.93	83.98
Total System Efficiency		[%]	88.72	87.49	80.11

As shown in Fig. 2, the path to the auxiliary DC load is in a parallel branch with the path to the main AC load. The power flow to the main AC load is decided by the SVM voltage pattern at the inverter output, and this is not affected after the path to the auxiliary DC load is connected. However, when α is regulated to decrease the CM power flow, the switching harmonics in SVM are shifted from CM to DM, and DM harmonics cannot be cancelled in line voltages of the main AC load. This will result in DM current ripples in the main AC load.

It can also be observed that, due to the additional power consumed by the auxiliary DC load, the current going through the inverter increases. Hence in practical implementations, the inverter should be dimensioned considering the peak power as the sum of the expected peak power of both the AC and DC loads. However, it should be noted that in many applications, the peak power consumption of the auxiliary DC load does not necessarily occur simultaneously as that of the main AC load. For example, if the proposed method is applied in the powertrain of a vehicle and the traction motor operates at peak power, the charging of the LV battery through the auxiliary DC output can be temporarily reduced. After the power consumption of the traction motor reduces, the LV battery charging rate can increase again.

E.   Impact on Inverter Efficiency

From the results presented in Section IV.C and IV.D, it can be concluded that it is possible to extract the CM switching harmonics and use them to power an auxiliary dc load. To investigate whether the harmonic extraction would have an impact on the efficiency of the inverter, two tests are conducted. Firstly, the inverter is only connected to a three-phase RL load. In each phase, the resistance is 2.21 Ω and the inductance is 219 µH. Thereafter, the CM harmonic extraction branch and the auxiliary dc load are connected in parallel with the original three-phase RL load. In both cases, the dc-link voltage is 200 V and the switching frequency is 30 kHz. The SVM is fixed to $k_7 = 0.5$ and $\alpha = 0°$, while m_a is swept from 0 to 0.9 with step of 0.1 and an additional point of 0.95. The inverter efficiency in both cases is calculated as

$$\eta = \frac{P_{inv.out}}{P_{inv.in}} \times 100\% = \frac{\sum_{i=1}^{N_{sin}} p_{inv.out}}{\sum_{i=1}^{N_{sin}} p_{inv.in}} \times 100\% \quad (38)$$

using the voltage and current measurements, where

$$p_{inv.out} = u_{inv.a} \cdot i_{inv.a} + u_{inv.b} \cdot i_{inv.b} + u_{inv.c} \cdot i_{inv.c}$$
$$p_{inv.in} = u_{inv.dc} \cdot i_{inv.dc} \quad (39)$$

and N_{sin} is the number of samples taken over an integer number of fundamental cycles. The results are shown in Fig. 18. The maximum inverter input power reaches 7.15 kW. The maximum power delivered to the auxiliary DC load reaches 1 kW. The percentage of auxiliary load power consumption with respect to the total power consumption on both loads is shown in green. As can be seen, the curve decreases as m_a increases. The efficiency difference at different inverter input power levels and different percentages of auxiliary load power consumption is generally below 0.5%. Hence the influence of the extraction circuit on the inverter efficiency is minor.

— Efficiency when only Three-Phase Load is connected
— Efficiency when both Three-Phase Load & Auxiliary DC Load are connected
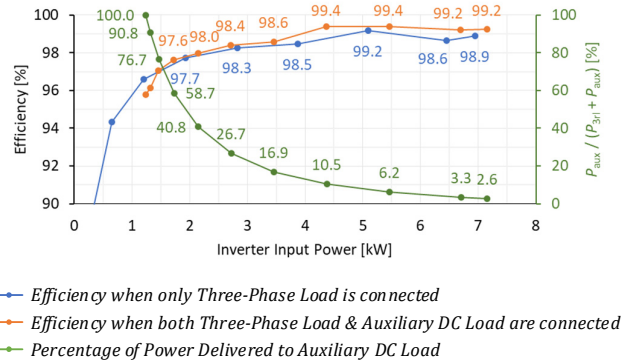— Percentage of Power Delivered to Auxiliary DC Load

Fig. 18   Experimental comparison of inverter efficiency between the cases with and without the auxiliary dc load

V. Conclusions

Common mode switching harmonics of a three-phase inverter can be extracted and rectified to power an auxiliary dc load. In this study, a control method and a circuit topology are proposed to realize this idea even without access to the neutral point of the three-phase load. The auxiliary dc output voltage is dependent on common mode switching harmonic contents which can be further controlled by regulating SVM switching patterns.

To physically implement the common mode power flow, an extraction circuit is proposed where the common mode switching harmonics of the inverter are extracted, rectified, and delivered to the auxiliary dc load. In the extraction circuit, a common mode passing coil in resonance with series-connected capacitors is employed and the resonance is tuned at the switching frequency.

An experimental setup is constructed to verify the circuit and control. The auxiliary dc output voltage reaches the maximum when the zero states share the same duty cycle within one switching period. The output voltage can be scaled down evenly when an angle shift α is introduced between the carrier waves for all three phases. The scaling factor is analytically found out to be $\frac{1+2\cdot\cos\alpha}{3}$. The efficiency of the CM power flow branch, including extraction circuit, transformer and diode rectifier, reaches 93.18% in the experimental prototype. The experimental results closely follow the analytical results. This shows that the proposed method works as expected. In the end, the impact of harmonic extraction on the efficiency of the inverter is investigated. In the test, the inverter input power reaches 7.15 kW and the inverter efficiency stabilizes around 99%. The efficiency is not significantly affected when the auxiliary load is connected.

VI. References

[1] International Energy Agency, "Global EV Outlook 2020," International Energy Agency, 2020.

[2] A. Emadi, Y. J. Lee and K. Rajashekara, "Power Electronics and Motor Drives in Electric, Hybrid Electric, and Plug-In Hybrid Electric Vehicles," *IEEE Transactions on Industrial Electronics,* vol. 55, no. 6, pp. 2237 - 2245, 2008.

[3] C. Stancu, T. Ward, K. M. Rahman, R. Dawsey and P. Savagian, "Separately Excited Synchronous Motor With Rotary Transformer for Hybrid Vehicle Application," *IEEE Transactions on Industry Applications,* vol. 54, no. 1, pp. 223-232, 2018.

[4] J. Tang, Y. Liu and N. Sharma, "Modeling and Experimental Verification of High-Frequency Inductive Brushless Exciter for Electrically Excited Synchronous Machines," *IEEE Transactions on Industry Applications,* vol. 55, no. 5, pp. 4613 - 4623, 2019.

[5] Y. Zhou and H. Nian, "Zero-Sequence Current Suppression Strategy of Open-Winding PMSG System With Common DC Bus Based on Zero Vector Redistribution," *IEEE Transactions on Industrial Electronics,* vol. 62, no. 6, pp. 3399 - 3408, 2015.

[6] L. Rovere, A. Formentini, G. L. Calzo, P. Zanchetta and T. Cox, "Zero-Sequence Voltage Elimination for Dual-Fed Common DC-Link Open-End Winding PMSM High-Speed Starter–Generator—Part I: Modulation," *IEEE Transactions on Industry Applications,* vol. 55, no. 6, pp. 7804 - 7812, 2019.

[7] L. Rovere, A. Formentini, G. L. Calzo, P. Zanchetta and T. Cox, "Zero-Sequence Voltage Elimination for Dual-Fed Common DC-Link Open-End Winding PMSM High-Speed Starter-Generator—Part II: Deadtime Hysteresis Control of Zero-Sequence Current," *IEEE Transactions on Industry Applications,* vol. 55, no. 6, pp. 7813 - 7821, 2019.

[8] X. Xing, X. Li, C. Qin, J. Chen and C. Zhang, "An Optimized Zero-Sequence Voltage Injection Method for Eliminating Circulating Current and Reducing Common Mode Voltage of Parallel-Connected Three-Level Converters," *IEEE Transactions on Industrial Electronics,* vol. 67, no. 8, pp. 6583 - 6596, 2020.

[9] J. Liu, X. Qin and Z. Yang, "Analysis of Zero-Sequence Circulating Current in Parallel PWM Inverter System with Difference of Carrier Wave Phases," in *Informatics in Control, Automation and Robotics*, Springer-Verlag, 2012, pp. 453 - 463.

[10] Ó. López, J. Álvarez, J. Malvar, A. G. Yepes, A. Vidal, F. Baneira, D. Pérez-Estévez, F. D. Freijedo and J. Doval-Gandoy, "Space-Vector PWM With Common-Mode Voltage Elimination for Multiphase Drives," *IEEE Transactions on Power Electronics,* vol. 31, no. 12, pp. 8151 - 8161, 2016.

[11] T. J. Dougherty, "Dual Voltage Alternator Using Center-Tap Regulation". United States Patent US6392348B1, 17 November 2000.

[12] J. Hsu, G.-J. Su, D. Adams, J. Nagashima, C. Stancu, D. Carlson and G. Smith, "Utilizing Zero-Sequence Switchings for Reversible Converters". United States Patent US20040004852A1, 03 July 2002.

[13] M. Senol and R. W. D. Doncker, "Drivetrain integrated dc-dc converter utilizing the zero sequence current of the starter-generator in 48V network vehicles," in *2015 Intl Aegean Conference on Electrical Machines & Power Electronics (ACEMP), 2015 Intl Conference on Optimization of Electrical & Electronic Equipment (OPTIM) & 2015 Intl Symposium on Advanced Electromechanical Motion Systems (ELECTROMOTION)*, Side, Turkey, 2015.

[14] T. Shukla, "Simulating & Evaluating Feasibility to Integrate Charging of 12V Battery with 48V Drivetrain for Dual Voltage 48V/12V Mild Hybrid Vehicles," Chalmers University of Technology, Gothenburg, 2017.

[15] D. G. Holmes and T. A. Lipo, "Zero Space Vector Placement Modulation Strategies," in *Pulse Width Modulation for Power Converters: Principles and Practice*, Wiley-IEEE Press, 2003, pp. 259 - 336.

[16] G. V. Stanke, H. W. v. d. Broeck and H.-C. Skudelny, "Analysis and Realization of a Pulsewidth Modulator Based on Voltage Space Vectors," *IEEE Transactions on Industry Applications,* vol. 24, no. 1, pp. 142 - 150, 1988.

[17] W. C. Duesterhoeft, M. W. Schulz and E. Clarke, "Determination of Instantaneous Currents and Voltages by Means of Alpha, Beta, and Zero Components," *Transactions of the American Institute of Electrical Engineers,* vol. 70, no. 2, pp. 1248 - 1255, 1951.

[18] R. L. Steigerwald, "A Comparison of Half-Bridge Resonant Converter Topologies," *IEEE Transactions on Power Electronics,* vol. 3, no. 2, pp. 174 - 182, 1988.

[19] Ferroxcube, "3C90 Material Specification," 01 September 2008. [Online]. Available: https://www.ferroxcube.com/upload/media/product/file/MDS/3c90.pdf. [Accessed 13 May 2021].

[20] Y. Liu, D. Pehrman, O. Lykartsis, J. Tang and T. Liu, "High frequency exciter of electrically excited synchronous motors for vehicle applications," in *2016 XXII International Conference on Electrical Machines (ICEM)*, Lausanne, Switzerland, 2016.

VII.   Biographies

Junfei Tang (S'16) received the B.Eng. degree in electrical engineering from Jiangsu University, Zhenjiang, China, in 2013, and the M.Sc and Ph.D degrees in electric power engineering from Chalmers University of Technology, Gothenburg, Sweden, in 2016 and 2021 respectively. Now he is a postdoctoral researcher in electric machines and power electronics in Chalmers University of Technology.

Daniel Pehrman (S'18) received the B.Sc., M.Sc. and PhD degrees in electric power engineering from the Chalmers University of Technology, Gothenburg, Sweden, in 2012, 2014, and 2021, respectively. He is currently working on electric vehicle charging towards heavy trucks with Sinix Electro AB in Gothenburg. His research interest includes inductive power transfer in electric vehicle applications, electric machine design, and power electronic devices.

Georgios Mademlis (S'15) received his Diploma of Engineering degree from the Faculty of Electrical and Computer Engineering, Aristotle University of Thessaloniki, Greece, in 2015. He obtained the Ph.D. degree in the area of SiC-based electric drives for renewable power generation and for automotive applications at Chalmers University of Technology, Gothenburg, Sweden, in 2021. He is currently working as a Postdoctoral researcher at the same institution. His research interests include renewable energy systems, design and control of power electronic converters and electrical machine drives.

Yujing Liu (SM'12) received the B.Sc., M.Sc. and Ph.D. degrees in electrical engineering from Harbin Institute of Technology, Harbin, China, in 1982, 1985, and 1988, respectively. In 1996-2013, he worked in ABB Corporate Research, Västerås, Sweden. Since 2013, he is a professor on electrical power engineering in Chalmers University of Technology. Gothenburg, Sweden. His interest includes research on motors, converters, and wireless charging for electric vehicles, generators and power electronics for tidal power conversion, and high efficiency machines for energy saving in industrial applications. Yujing Liu is a senior IEEE member and a member in Swedish Standard Committee on Electrical Machines.